ACS Photonics

Article

pubs.acs.org/journal/apchd5

Advanced Structural Engineering of Nanoporous Photonic Structures: Tailoring Nanopore Architecture to Enhance Sensing Properties

Tushar Kumeria,[†,§] Abel Santos,*[,†,§] Mohammad Mahbubur Rahman,[†,‡] Josep Ferré-Borrull,[‡] Lluís F. Marsal,[‡] and Dusan Losic[†]

[†]School of Chemical Engineering, The University of Adelaide, Adelaide, SA 5005, Australia

[‡]Departament d'Enginyeria Electrònica, Elèctrica i Automàtica, Universitat Rovira i Virgili, Avda Països Catalans 26, 43007 Tarragona, Spain

Supporting Information

ABSTRACT: In this study, we demonstrate that an optimal design of the pore geometry and shape of sensing platforms based on nanoporous anodic alumina (NAA) photonic structures is critical to develop optical sensors with improved capabilities. To this end, two types of NAA photonic structures featuring different pore geometries (i.e., pore lengths and diameters) and shapes (i.e., straight and modulated pores) were produced, and their optical characteristics were assessed systematically by reflectometric interference spectroscopy. The geometric features (i.e., pore lengths, diameters, and shapes) were systematically modified in order to establish the optimization paths for the sensitivity, low limit of detection, and linearity of these optical sensing platforms. The obtained results reveal that an optimal design of these nanoporous photonic structures can enhance their sensitivity, achieve a lower limit of detection, and improve their linearity for both nonspecific and specific detection of analytes. Therefore, as this study demonstrates, the rational design of optical nanoporous sensing platforms is critical in the development of reliable, sensitive, robust, inexpensive, and portable optical systems for a broad range of sensing applications.

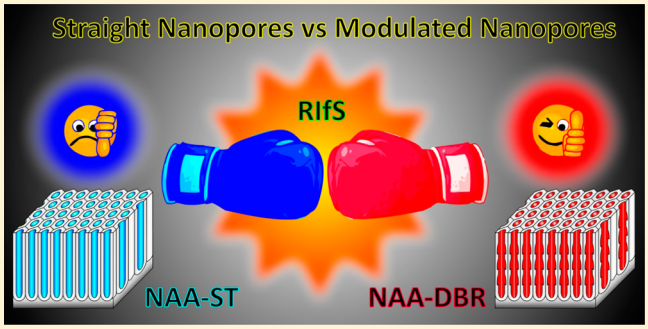

KEYWORDS: *nanoporous anodic alumina, photonics, structural engineering, pore geometry, reflectometric interference spectroscopy*

Currently, optical sensing devices are present in more places of our ordinary lives than ever before. As an example, the advent of smart phones has devised a plethora of new possibilities toward the development of all-in-one analytical devices for real-life applications, which could range from water quality analysis (e.g., detection of levels of heavy metal ions in water) to self-diagnosis (e.g., quantification of levels of glucose in blood).[1−4] Although this technology is still at its beginnings, more exciting developments are expected to be done in the next years. Before this technology becomes feasible and reliable, however, more extensive fundamental research must be carried out in order to make individual components efficient, reliable, sensitive, selective, and inexpensive.

Basically, an optical sensor is composed of a light source, where the optical wave is generated, a sensing platform, where the interaction between light and matter takes place, and a detector, which measures the optical signal shift (i.e., sensing principle).[5] Among these components, the sensing platform plays a critical role as light interacts with analyte molecules present in its effective medium, producing quantifiable changes in the characteristic optical signal of the sensing platform. Subsequently, these changes can be quantitatively (concentration) and/or qualitatively (spectral signature) estimated by the detector. Typically, sensing platforms are based on optically active or passive materials, the function of which is to guide, reflect, absorb, transmit, emit, or enhance the incident light emitted by the source. As far as the different materials used to develop optical sensing platforms is concerned, nanomaterials have enabled the development of highly sensitive and sophisticated systems such as surface-enhanced Raman spectroscopy (SERS), surface plasmon resonance spectroscopy (SPR), localized surface plasmon resonance spectroscopy (LSPR) and others.[6−15] These optical techniques can achieve detection limits as low as single molecules through the amplification of electromagnetic fields generated by the excitation of localized surface plasmons.[16] Another example of a sensitive optical technique extensively used to develop optical sensors is reflectometric interference spectroscopy (RIfS).[17−19] RIfS relies on the constructive interference of reflected light, which takes place when a white light beam interacts with a thin

Received: August 27, 2014
Published: November 17, 2014

 © 2014 American Chemical Society

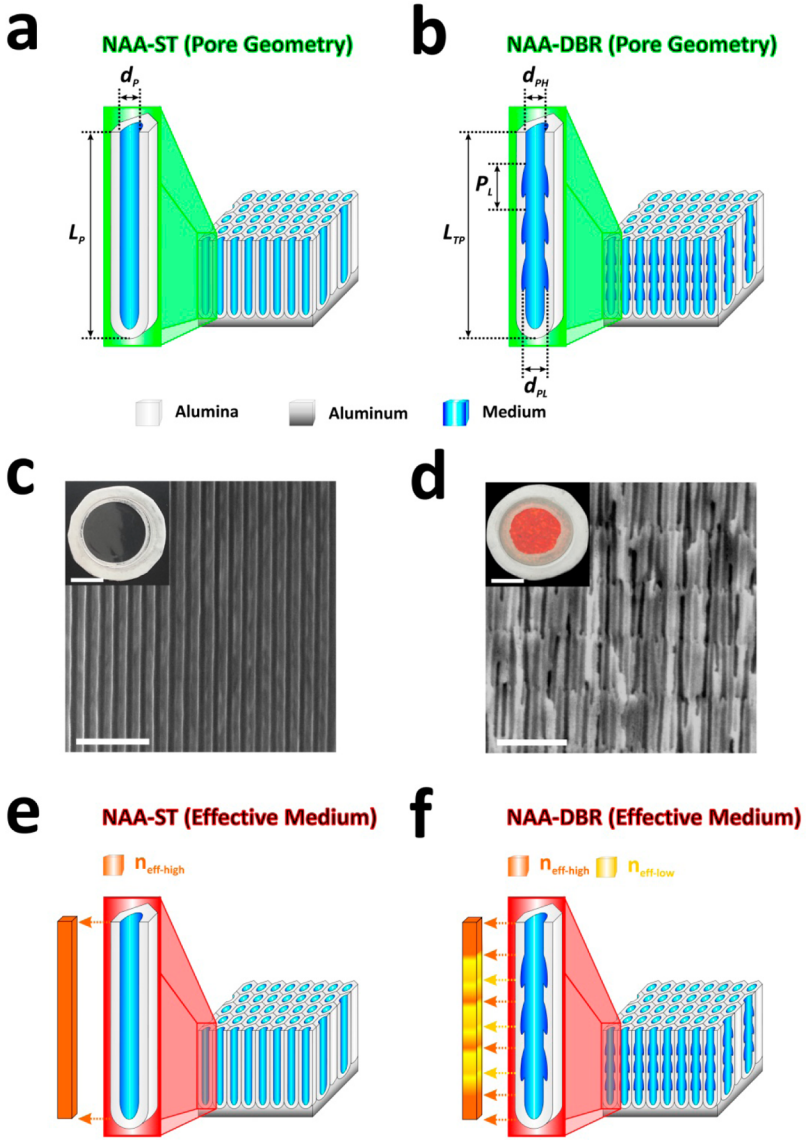

Figure 1. Structural and optical characteristics of photonic structures based on nanoporous anodic alumina. (a, b) Illustrations depicting the representative geometric features of NAA-ST and NAA-DBR platforms, respectively. (c, d) Cross-section SEM images of NAA-ST and NAA-DBR photonic structures, respectively (scale bars = 500 nm). The insets show digital images of these photonic structures after the aluminum substrate was selectively removed from the back side by chemical etching (scale bar = 0.5 cm). (e, f) Schemes showing the relationship between the effective medium and the pore geometry in NAA-ST and NAA-DBR platforms, respectively.

film. This optical technique, which is typically implemented into low-cost miniature spectrometers, can be combined with nanoporous materials such as nanoporous anodic alumina (NAA) in order to develop highly sensitive and reliable optical sensing systems.[20−23] NAA is a nanoporous material produced by electrochemical anodization of aluminum and presents many interesting advantages for the development of optical sensing platforms.[24−28] Some assets of NAA are a cost-competitive and industrially scalable fabrication process, stable optical signals without passivation, controllable and versatile pore geometry, chemical and physical stability, mechanical robustness, easy chemical functionalization, and the capability to guide, reflect, transmit, emit, and enhance incident light by engineering its nanoporous structure through different anodization approaches.[29,30] For these reasons, NAA has been recently envisaged for the development of low-cost, portable, and highly sensitive optical sensing platforms featuring up-to-the-minute capabilities.[31−33] Regardless of the recent use of NAA as a sensing platform, more extensive fundamental research must be carried out in order to establish the optimization paths toward NAA photonic structures with improved optical properties for sensing applications.

Herein we present a detailed study assessing the optical characteristics and sensing performances of two types of NAA photonic structures featuring different pore geometries and shapes. Our study demonstrates that the sensing properties of these photonic structures can be substantially improved by engineering their nanoporous structure.

RESULTS AND DISCUSSION

Fabrication and Structural Characterization of NAA Photonic Structures. Figure 1 illustrates the structures of the two different types of NAA sensing platforms assessed in this study, which were fabricated by electrochemical anodization of aluminum chips under potentiostatic conditions. The former

dx.doi.org/10.1021/ph500316u | ACS Photonics 2014, 1, 1298−1306

type of NAA photonic structure, straight NAA (NAA-ST), was produced by anodizing aluminum chips at constant voltage through a symmetric two-step anodization approach.[24−28] NAA-ST samples featured straight cylindrical nanopores from top to bottom and thus constant effective refractive index (n_{eff}) along the nanopores. The latter type of NAA photonic structure, NAA distributed Bragg reflector (NAA-DBR), featured a modulated pore diameter in depth and was produced by a pseudosinusoidal anodization profile (i.e., shifting between high and low anodization voltages) through a modified two-step approach reported elsewhere.[34,35] These NAA photonic structures presented a modulated effective refractive index in depth that was switched between high ($n_{eff\text{-}high}$, low anodization voltage) and low ($n_{eff\text{-}low}$, high anodization voltage) by means of the anodization profile. More detailed information on the fabrication processes of the NAA-ST and NAA-DBR platforms is included in Methods and Figure S1 in the Supporting Information.

The pore lengths of NAA-ST and NAA-DBR platforms were set to four different values (i.e., 30, 35, 40, and 45 μm) by modifying the time of the second anodization step (t_{AN}). It should be noted that in the case of NAA-DBR these pore lengths corresponded to 125, 150, 175, and 200 periods, respectively. Furthermore, the nanopores of as-produced NAA-ST and NAA-DBR platforms were widened by wet chemical etching to obtain four different pore diameters, which corresponded to four different pore widening time lengths (i.e., t_{PW} = 0, 8, 16, and 24 min). Therefore, a total of 16 samples of each type of NAA structure were used in this study, allowing us to assess the sensing characteristics of these photonic structures as a function of their pore geometry and shape within the aforementioned range of geometric features. As far as the different geometric features of these platforms is concerned, whereas the structure of NAA-ST can be defined by the pore length (L_P) and the pore diameter (d_P), the geometric features of NAA-DBR are the total pore length (L_{TP}), the pore diameters, which vary periodically from big to small according to the periodic high and low effective refractive indexes, respectively (d_{PH} with $n_{eff\text{-}high}$ and d_{PL} with $n_{eff\text{-}low}$), and the period length (P_L) (Figure 1a,b). The different geometric characteristics of the NAA-ST and NAA-DBR platforms were established by scanning electron microscopy (SEM) image analysis, and Table 1 summarizes the relationships between fabrication parameters and geometric features.[36]

Table 1. Fabrication Parameters and Geometric Features of NAA-ST and NAA-DBR Photonic Structures Assessed in This Study

NAA-ST			
t_{AN} (h)	L_P (μm)	t_{PW} (min)	d_P (nm)
9.5	30 ± 1	0	21 ± 2
11.3	35 ± 1	8	31 ± 1
13.0	40 ± 1	16	44 ± 2
14.5	45 ± 1	24	56 ± 1

NAA-DBR					
period	L_{PT} (μm)	P_L (nm)	t_{PW} (min)	d_{PH} (nm)	d_{PL} (nm)
125	30 ± 1	171 ± 14	0	18 ± 3	30 ± 4
150	35 ± 1	171 ± 14	8	21 ± 4	38 ± 6
175	40 ± 1	171 ± 14	16	31 ± 3	49 ± 4
200	45 ± 1	171 ± 14	24	42 ± 3	69 ± 9

Figure 1c,d shows cross-section SEM images of the resulting NAA-ST and NAA-DBR structures as well as digital images of these NAA photonic structures. Figure 1c reveals that the NAA-ST structures featured cylindrical nanopores from top to bottom and were transparent, allowing light to pass through so that objects behind were distinctly seen (Figure 1c inset). However, as Figure 1d shows, NAA-DBR platforms presented periodically modulated pore diameters in depth and had red color due to structural coloring associated with light reflection phenomenon (Figure 1d inset).[37] It is worthwhile to note that the structure of the NAA-DBR platform can be tuned in order to reflect light at specific wavelengths within the visible light range.[38] This can be achieved by applying different anodization profiles and by pore widening, which are translated into the nanoporous structure of the photonic platform and thus into its effective refractive index (Figure 1e,f).

Sensing Principles and Optical Assessment of NAA-ST and NAA-DBR Photonic Structures. *Sensing Principles.* Figure 2a,b depicts the sensing principles of NAA-ST and NAA-DBR platforms after their nanopores were infiltrated with water and ethanol. It is well-known that an increment of the effective medium of nanoporous films leads to a red shift in their RIfS spectra (i.e., a shift toward longer wavelengths). In the case of NAA-ST platforms, this shift can be quantified by means of the effective optical thickness change (ΔOT_{eff}), which can be calculated by applying a fast Fourier transform (FFT) to the RIfS spectrum.[39−41] As far as the sensing principle in NAA-DBR platforms is concerned, this is based on changes in the characteristic reflection peak position ($\Delta\lambda_{peak}$) in their RIfS spectra.[42,43] In our study, we used these sensing principles in order to evaluate the optical characteristics of these photonic structures and find the optical optimization paths toward NAA platforms with optimized properties for sensing purposes in the UV−vis range. It should be noted that in the context of our study, the optical optimization paths for the sensing characteristics of NAA-ST and NAA-DBR structures were established using a total of 16 samples of each type of NAA photonic structure.

Optical Assessment under Nonspecific Adsorption Conditions. To assess the optical properties of the NAA-ST and NAA-DBR photonic platforms under nonspecific adsorption conditions, we modified the effective medium of these nanoporous structures by infiltrating their nanopores with different aqueous solutions of glucose ($C_6H_{12}O_6$) (i.e., 0.01, 0.05, 0.1, 0.2, 0.5, and 1.0 M), which provided different levels of refractive index (i.e., 1.333, 1.334, 1.336, 1.339, 1.349, and 1.363 refractive index units (RIU), respectively). In this process, the RIfS spectra of these NAA platforms were monitored in real time using a flow cell combined with a RIfS system (Figure 2c). Glucose solutions were flowed through the flow cell, where the NAA platforms were placed, and changes in the effective medium of these photonic structures produced shifts in their RIfS spectra. These changes, monitored in real time, were recorded and converted into ΔOT_{eff} and $\Delta\lambda_{peak}$, which were subsequently assessed in order to establish and compare the different optical characteristics of NAA-ST and NAA-DBR photonic structures, respectively. Examples of real-time monitoring of ΔOT_{eff} and $\Delta\lambda_{peak}$ are included in Figure S2 in the Supporting Information.

Figure 3 summarizes the obtained results, showing the linear fits between the optical parameters (i.e., ΔOT_{eff} and $\Delta\lambda_{peak}$ for the NAA-ST and NAA-DBR platforms, respectively) and the refractive indexes of glucose solutions as a function of the pore

dx.doi.org/10.1021/ph500316u | ACS Photonics 2014, 1, 1298−1306

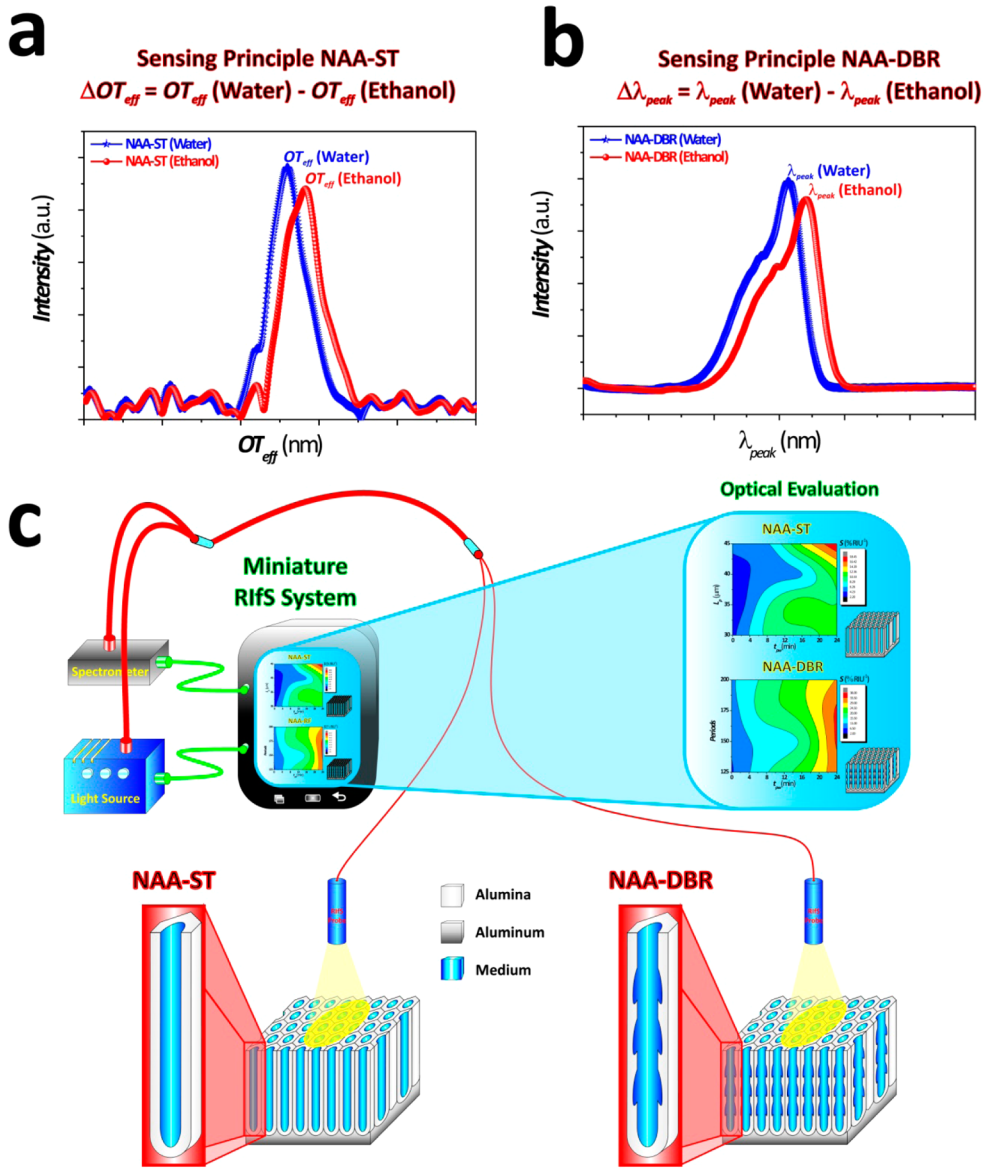

Figure 2. Sensing principles and experimental setup used in this study to assess the optical characteristics of NAA photonic structures. a-b) Sensing principles of NAA-ST and NAA-DBR photonic structures in RIfS based on changes in the effective optical thickness (ΔOT_{eff}) and shifts in the characteristic peak position ($\Delta\lambda_{peak}$), respectively. c) Experimental optical setup composed of tablet, light source, spectrometer, optical probes and NAA photonic structures.

length (i.e., the number of periods for NAA-DBR platforms) and the pore widening time. At first sight it is observed that the sensitivity of these photonic structures (i.e., the slope of the linear fit) increases with the pore widening time (i.e., bigger pores). In order to gain insight into these results, find out the optimization paths, and provide an objective comparison between these two photonic structures, we expressed changes in OT_{eff} and λ_{peak} in terms of percentage. Figure 4 presents contour plots of the different sensing characteristics (i.e., sensitivity (S), low limit of detection (LoD), and linearity (R^2)) of NAA-ST and NAA-DBR platforms along with the optimization paths for each of these parameters. Likewise in a topographic map, each optimization path was established by following the path with the highest slope between the lowest and highest values of the corresponding sensing parameter. Table 2 summarizes the geometric characteristics of these NAA-ST and NAA-DBR platforms, presenting the most optimal optical characteristics obtained from this analysis.

Figure 4a,b shows the dependence of the sensitivity on the pore length (i.e., number of cycles for NAA-DBR platforms) and the pore widening time for NAA-ST and NAA-DBR platforms, respectively. It is observed that in terms of sensitivity the two photonic structures present similar patterns of dependence with these geometric features. In other words, the lines between color fields are closer to each other in a similar manner and the distribution of color fields is fairly homogeneous in both cases, indicating that S changes smoothly with the pore geometry. Nevertheless, the sensitivity of NAA-DBR platforms (i.e., 34.35 ± 1.16% RIU^{-1}) is almost 2-fold higher than that of NAA-ST platforms (i.e., 18.42 ± 0.35% RIU^{-1}). Furthermore, the white arrows in Figure 4a,b depict the sensitivity optimization paths in NAA-ST and NAA-DBR photonic structures. From this, we established the highest sensitivities for NAA-ST and NAA-DBR platforms, which were achieved at (L_P = 45 ± 1 μm ; t_{PW} = 24 min) and (L_{TP} = 40 ± 1 μm (175 periods); t_{PW} = 24 min), respectively.

dx.doi.org/10.1021/ph500316u | ACS Photonics 2014, 1, 1298−1306

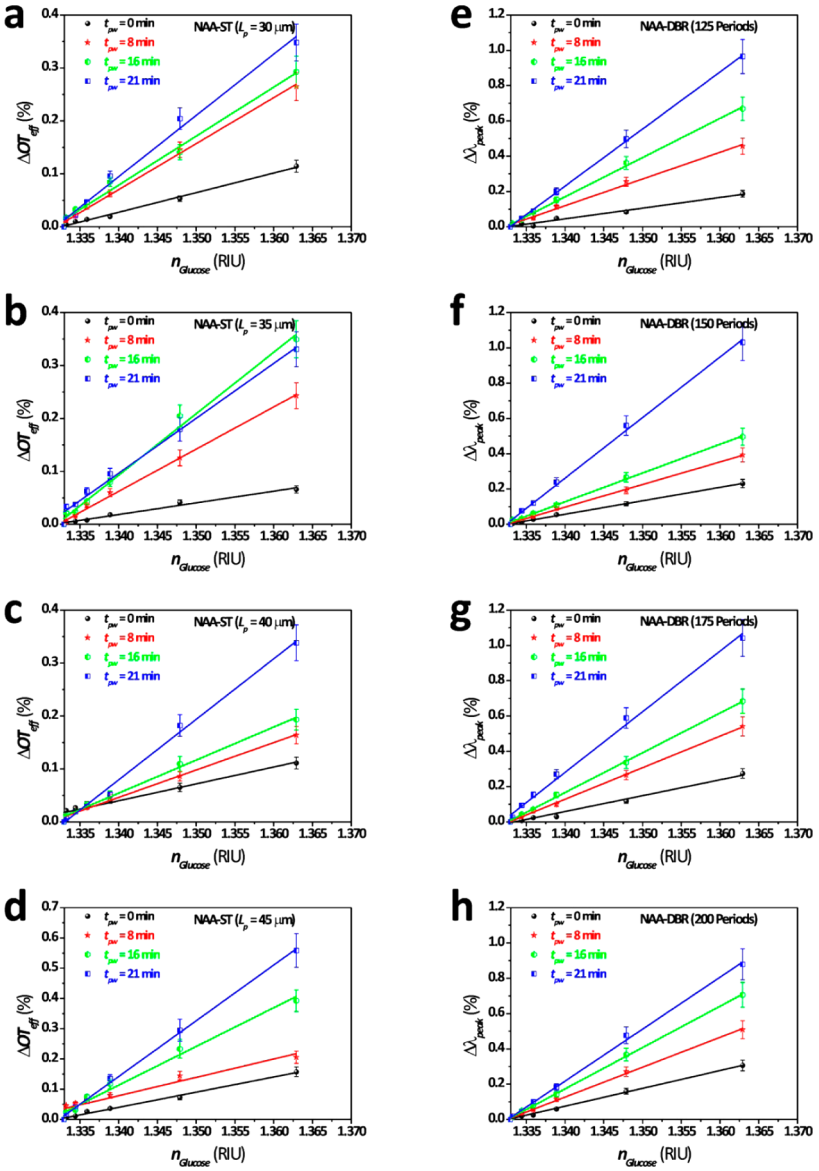

Figure 3. Optical assessment of (a–d) NAA-ST and (e–h) NAA-DBR photonic structures by measuring ΔOT_{eff} and $\Delta\lambda_{peak}$, respectively, as functions of the geometric characteristics and the refractive index of glucose solutions.

As far as the low limit of detection is concerned, Figure 4c,d illustrates the dependence of LoD (calculated as 3σ and expressed in RIU) on the pore length and the pore widening time for NAA-ST and NAA-DBR photonic structures, respectively. These contour plots show that both NAA structures present primary and secondary optimization paths and that the dependence of the LoD on the geometric features of NAA-ST and NAA-DBR is much more heterogeneous than that shown for S (i.e., heterogeneous distribution of color fields). In the case of NAA-ST platforms, the lowest LoD value (i.e., 0.084 RIU) is achieved at (L_P = 45 ± 1 μm; t_{PW} = 24 min), with a secondary minimum of LoD (i.e., 0.103 RIU) at (L_p = 30 ± 1 μm; t_{PW} = 8 min). For NAA-DBR platforms, the lowest LoD value (i.e., 0.040 RIU) is obtained at (L_{TP} = 30 ± 1 μm (125 periods); t_{PW} = 24 min), with a secondary LoD minimum (i.e., 0.052 RIU) at (L_{TP} = 45 ± 1 μm (200 periods); t_{PW} = 16 min). Again, these results verify that NAA-DBR photonic structures can achieve much lower LoD than NAA-ST platforms.

Figure 4e,f depicts the relationship between the linearity and the pore geometry for NAA-ST and NAA-DBR platforms, respectively. As in the case of the LoD, these contour plots reveal that both NAA platforms present primary and secondary optimization paths and a heterogeneous distribution of color fields with the geometric features. The highest linearity in NAA-ST platforms (i.e., 0.998) is achieved at (L_P = 45 ± 1 μm; t_{PW} = 24 min), with a secondary maximum (i.e., 0.997) at (L_P = 35 ± 1 μm; t_{PW} = 8 min). In the case of NAA-DBR photonic structures, R^2 achieves its highest value (i.e., 0.999) at (L_{TP} = 45 ± 1 μm (200 periods); t_{PW} = 8 min), with a secondary maximum (i.e., 0.999) at (L_{TP} = 40 ± 1 μm (175 periods); t_{PW} = 0 min). Although both sensing platforms present excellent linearity, these results verify that NAA-DBR platforms are slightly more linear than NAA-ST platforms.

Optical Assessment under Specific Adsorption Conditions. Finally, NAA-ST and NAA-DBR photonic platforms were assessed when detecting mercury ions (Hg^{2+}) in water under specific adsorption conditions. To this end, the surface of these

dx.doi.org/10.1021/ph500316u | ACS Photonics 2014, 1, 1298–1306

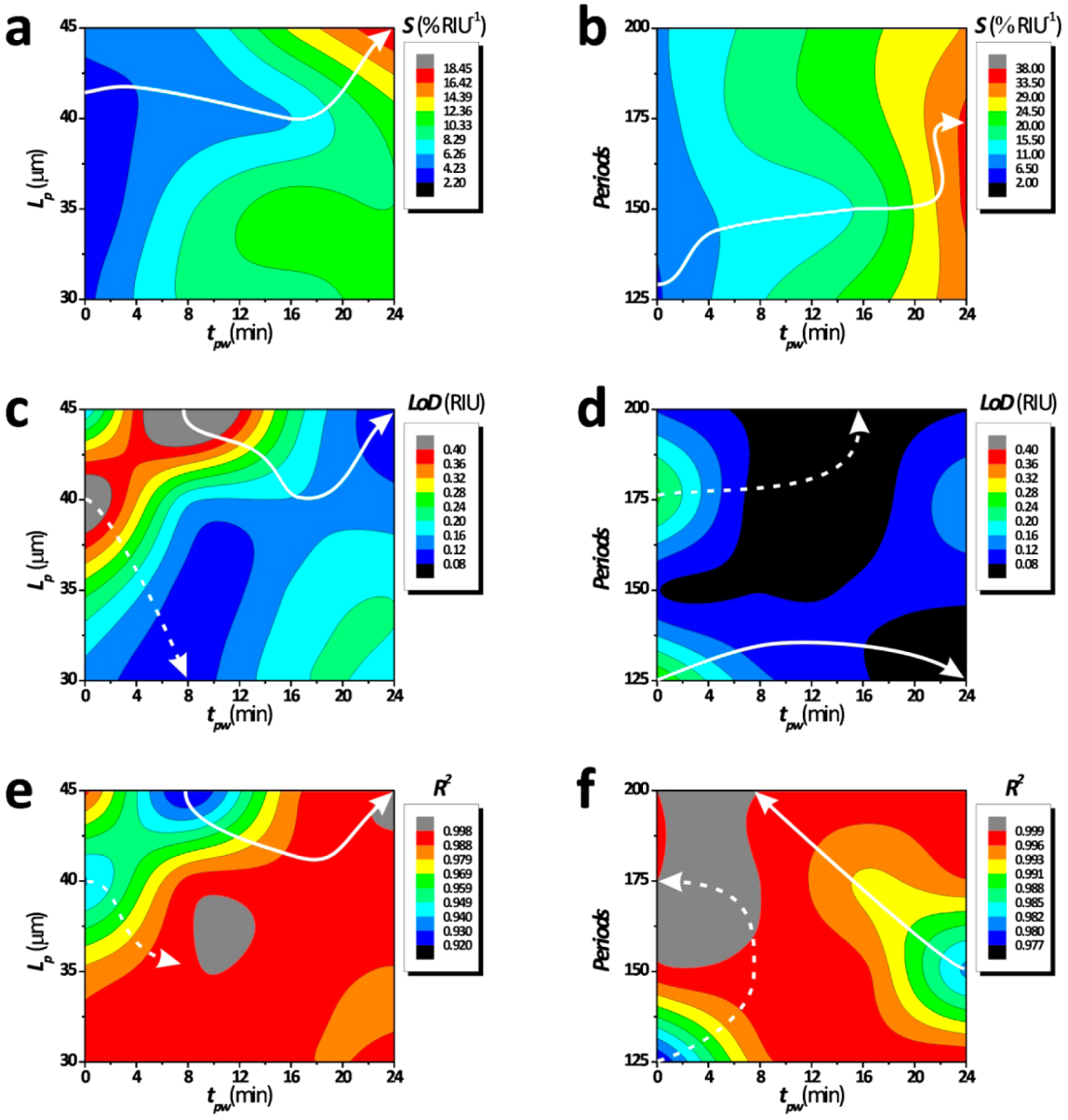

Figure 4. Contour plots showing the optical optimization paths for sensitivity (S), low limit of detection (LoD), and linearity (R^2) in (a, c, e) NAA-ST and (b, d, f) NAA-DBR photonic structures as assessed by RIfS: (a, b) sensitivity in terms of change in sensing parameter (i.e., ΔOT_{eff} or $\Delta\lambda_{peak}$), expressed in percentage per refractive index unit; (c, d) low limit of detection, calculated as 3σ and expressed in refractive index units; (e, f) linearity, calculated as the correlation coefficient. White arrows denote the different optimization paths for S, LoD, and R^2 (solid lines = primary optimization paths and dashed lines = secondary optimization paths).

Table 2. Summary of Geometric and Optical Characteristics of NAA-ST and NAA-DBR Photonic Structures with the Best Optical Performance

optical platform	optical parameter	value	geometric features
NAA-ST	S	18.42 ± 0.35 % RIU^{-1}	L_P = 45 ± 1 μm; d_P = 56 ± 1 nm
NAA-DBR	S	34.35 ± 1.16 % RIU^{-1}	L_{TP} = 40 ± 1 μm (175 periods); d_{PH} = 42 ± 3 nm; d_{PL} = 69 ± 9 nm
NAA-ST	LoD	0.084 RIU	L_P = 45 ± 1 mm ; d_P = 56 ± 1 nm
NAA-DBR	LoD	0.040 RIU	L_{TP} = 30 ± 1 μm (125 periods); d_{PH} = 42 ± 3 nm; d_{PL} = 69 ± 9 nm
NAA-ST	R^2	0.998	L_P = 45 ± 1 mm; d_P = 56 ± 1 nm
NAA-DBR	R^2	0.999	L_{TP} = 45 ± 1 μm (200 periods); d_{PH} = 21 ± 4 nm; d_{PL} = 38 ± 6 nm

NAA structures was functionalized via silanization with thiol functional groups through a well-established protocol reported elsewhere[44] (see Methods). This modification endowed these sensing platforms with chemical selectivity toward ionic mercury, which was achieved by the affinity between thiol groups and mercury ions (Figure 5a). Six different concentrations of mercury ions were used in this study (i.e., 1, 5, 10, 20, 40, and 80 μM), and the geometric features of the photonic platforms assessed in this study were set to L_P = 35 ± 1 μm and d_P = 44 ± 2 nm for NAA-ST and L_{TP} = 35 ± 1 μm (150

dx.doi.org/10.1021/ph500316u | ACS Photonics 2014, 1, 1298−1306

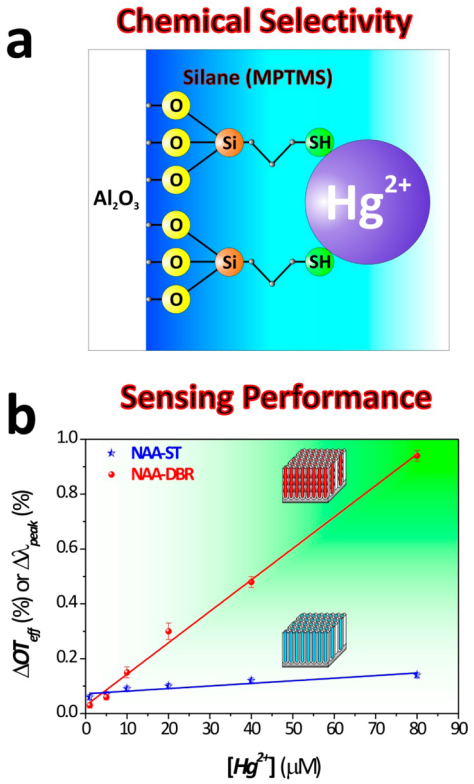

Figure 5. Optical assessment of NAA-ST and NAA-DBR photonic structures by RIfS in detection of mercury ions (Hg^{2+}) in water. (a) Scheme illustrating the surface chemistry modification using thiol chemistry to endow NAA-ST and NAA-DBR photonic structures with chemical selectivity toward ionic mercury. (b) Calibration curves showing the sensing performance of NAA-ST and NAA-DBR photonic structures as a function of the analyte concentration ($[Hg^{2+}]$).

periods), d_{PH} = 31 ± 3 nm, and d_{PL} = 49 ± 4 nm for NAA-DBR. As Figure 5b shows, the sensing performance of NAA-DBR photonic structures was found to be significantly better than that of NAA-ST platforms. Table 3 summarizes the

Table 3. Summary of the Sensing Characteristics of NAA-ST and NAA-DBR Photonic Structures Assessed for the Detection of Ionic Mercury in Water

optical platform	S (% μM^{-1})[a]	LoD (μM)	R^2
NAA-ST	0.0009 ± 0.0002	22.82	0.854
NAA-DBR	0.0115 ± 0.0004	4.20	0.994

[a]Sensitivity expressed in terms of the change in the corresponding sensing parameter (i.e., ΔOT_{eff} or $\Delta\lambda_{peak}$) in units of percentage per analyte concentration unit.

obtained results, which reveal that whereas NAA-DBR photonic structures present a sensitivity of 0.0115 ± 0.0004% μM^{-1}, NAA-ST structures have a 12-fold lower sensitivity of 0.0009 ± 0.0002% μM^{-1}. Furthermore, the low limit of detection of NAA-ST platforms (i.e., 22.82 μM/4.56 ppm) is almost 5-fold higher than that of NAA-DBR photonic structures (i.e., 4.20 μM/0.84 ppm). Finally, it was found that NAA-DBR structures present a more linear response with the analyte concentration (i.e., 0.994) than NAA-ST structures (i.e., 0.854). It is worthwhile to note that the lower limit of detection of these sensing platforms is higher than that established by the U.S. Environmental Protection Agency for drinking water (i.e., 2 ppb). However, we want to stress that the objective of our study was to demonstrate the ability of these photonic platforms to detect analytes under specific adsorption conditions. In that respect, there are many surface chemistry approaches that could enhance the sensing capabilities of these platforms. As an example, it has been demonstrated that different functional molecules (e.g., peptides, DNA, oligonucleotides, etc.) can provide much higher sensitivity than that of traditional thiol chemistry through bigger changes in the effective medium of the sensing platforms.[45,46]

CONCLUSION

In this study, we have demonstrated that an optimal design of the pore geometry and shape of photonic structures based on nanoporous anodic alumina can provide enhanced optical properties, which are fundamental requisites for the development of optical sensors with improved capabilities for broad sensing applications. The effects of the pore geometry and shape of two types of NAA photonic structures on their optical characteristics were systematically assessed. Furthermore, optimization paths for the sensitivity, low limit of detection, and linearity of these NAA photonic platforms were established and assessed under nonspecific and specific adsorption conditions for two different types of analytes.

The development of sensitive, reliable, robust, stable, cost-competitive, portable, and selective optical sensing systems requires photonic sensing platforms to have improved optical properties. This study has demonstrated that it is possible to enhance the sensitivity, low limit of detection, and linearity of these NAA photonic structures by engineering their nanopores. Undoubtedly, this reveals the importance of an optimized design of sensing platforms in the development of future sensing systems.

METHODS

Materials. High-purity (99.9997%) aluminum foils with a thickness of 0.32 mm were supplied by Goodfellow Cambridge Ltd. (UK). Oxalic acid ($C_2H_2O_4$), phosphoric acid (H_3PO_4), hydrochloric acid (HCl), ethanol (C_2H_5OH), perchloric acid ($HClO_4$), hydrogen peroxide (H_2O_2), chromium trioxide (CrO_3), 3-(mercaptopropyl)trimethoxysilane (MPTMS), D-glucose ($C_6H_{12}O_6$), and mercury(II) chloride ($HgCl_2$) were supplied by Sigma-Aldrich (Australia) and used without further purification. Aqueous solutions used in this study were prepared with ultrapure water (Option Q—Purelabs, Australia).

Fabrication of NAA-ST and NAA-DBR Photonic Structures. Prior to anodization, circular Al substrates with a diameter of 1.5 cm were cleaned under sonication in ethanol (EtOH) and distilled water for 15 min each. Subsequently, aluminum chips were electropolished in a 4:1 (v/v) mixture of EtOH and $HClO_4$ at 20 V and 5 °C for 3 min. After electropolishing, the first anodization step was carried out in a 0.3 M aqueous solution of $H_2C_2O_4$ at 40 V and 6 °C for 20 h. Then the resulting NAA layer was chemically removed in a mixture of 0.2 M chromic acid (H_2CrO_4) and 0.4 M H_3PO_4 at 70 °C for 3 h in order to pattern the aluminum surface and enable the growth of self-organized nanopores from top to bottom. As far as the second anodization step is concerned, two different electrochemical approaches were used to produce NAA-ST and NAA-DBR photonic platforms. Whereas the former type was produced by anodization under the

dx.doi.org/10.1021/ph500316u | ACS Photonics 2014, 1, 1298−1306

aforementioned conditions (i.e., 0.3 M $H_2C_2O_4$ at 40 V and 6 °C), the latter type was fabricated using the same conditions but applying a pseudosinusoidal anodization profile. This profile was started by an increasing voltage ramp from 20 to 50 V at a rate of 0.5 V s^{-1}. Then, the process was continued at 50 V for a charge of 1 C. Subsequently, the anodization voltage was linearly reduced from 50 to 20 V at a rate of −0.01 V s^{-1}. In the case of NAA-ST platforms, the second anodization step was controlled by time in order to produce NAA-ST platforms with thicknesses of 30, 35, 40, and 45 μm. However, in the case of NAA-DBR photonic structures, this anodization step was controlled by the number of cycles (i.e., 125, 150, 175, and 200 cycles), which corresponded to thicknesses of 30, 35, 40, and 45 μm, respectively. Finally, the remaining aluminum substrate was removed from the back side by wet etching in a mixture of hydrochloric acid and cupric chloride ($HCl/CuCl_2$), and the nanopores of NAA-ST and NAA-DBR photonic structures were widened by wet chemical etching in 5 wt % H_3PO_4 at 35 °C.

RIfS Setup. The optical characteristics of NAA-ST and NAA-DBR photonic structures were assessed using a RIfS system combined with a flow cell through which the different solutions of glucose and mercury ions were flowed by a peristaltic pump (BT100-2J, LongerPump, USA) at a constant flow rate of 400 μL min^{-1}. Briefly, this optical system was composed of a bifurcated optical probe that conducted and focused white light from a tungsten source (LS-1LL, Ocean Optics, USA). Light reflected from NAA-ST and NAA-DBR platforms was collected by the collection fiber, which was assembled around the optical probe and conducted the reflected light to a miniature spectrophotometer (USB 4000, Ocean Optics, USA). RIfS spectra in the 400−1000 nm wavelength range were acquired in real time and saved at intervals of 30 s with an integration time of 100 ms and 50 average measurements. These spectra were subsequently processed in Igor Pro library (Wavemetrics, USA).

Chemical Functionalization of NAA-ST and NAA-DBR Photonic Structures. The inner surfaces of the nanopores of NAA-ST and NAA-DBR photonic platforms were chemically modified with MPTMS following a well-established silanization protocol. Prior to functionalization, the number of hydroxyl groups (−OH) on the inner surfaces of NAA platforms was increased by boiling these nanoporous substrates in 30 wt % H_2O_2 for 10 min at 90 °C. After this, NAA platforms were dried under a nitrogen stream and functionalized via chemical vapor deposition of MPTMS at 135 °C for 3 h. Subsequently, NAA platforms were washed with acetone and water in order to remove physisorbed MPTMS molecules.

Structural Characterization of NAA-ST and NAA-DBR Photonic Structures. The morphologies and structures of NAA-ST and NAA-DBR platforms were characterized by SEM image analysis from images acquired using a field-emission-gun scanning electron microscope (FEG-SEM FEI Quanta 450).

■ ASSOCIATED CONTENT

Ⓢ Supporting Information

Further information on the anodization profiles used to produce NAA-ST and NAA-DBR photonic platforms and examples of real-time monitoring of ΔOT_{eff} and $\Delta\lambda_{peak}$ after infiltration with different glucose solutions. This material is available free of charge via the Internet at http://pubs.acs.org.

■ AUTHOR INFORMATION

Corresponding Author

*Phone: +61 8 8313 1535. Fax: +61 8 8303 4373. E-mail: abel.santos@adelaide.edu.au. Web: http://www.adelaide.edu.au/directory/abel.santos.

Author Contributions

§T.K. and A.S. contributed equally to this work and carried out the experimental part of this study. The resulting data were analyzed by all authors, and the manuscript was written through contributions of all authors. All authors have given approval to the final version of the manuscript.

Notes

The authors declare no competing financial interest.

■ ACKNOWLEDGMENTS

This research was supported by the Australian Research Council (ARC) through Grants DE14010054 and FT110100711, the Spanish Ministerio de Economía y Competitividad through Grant TEC2012-34397, and the Generalitat de Catalunya through the Grant 2014 SGR 1344. The authors also thank the School of Chemical Engineering (UoA) and Adelaide Microscopy (AM).

■ REFERENCES

(1) Wei, Q.; Nagi, R.; Sadeghi, K.; Feng, S.; Yan, E.; Ki, S. J.; Caire, R.; Tseng, D.; Ozcan, A. Detection and Spatial Mapping of Mercury Contamination in Water Samples Using a Smart-Phone. *ACS Nano* **2014**, *8*, 1121−1129.

(2) Wei, Q.; Qi, H.; Luo, W.; Tseng, D.; Ki, S. J.; Wan, Z.; Göröcs, Z.; Bentolila, L. A.; Wu, T. T.; Sun, R.; Ozcan, A. Fluorescent Imaging of Single Nanoparticles and Viruses on a Smart Phone. *ACS Nano* **2013**, *7*, 9147−9155.

(3) Khatua, S.; Orrit, M. Toward Single-Molecule Microscopy on a Smart Phone. *ACS Nano* **2013**, *7*, 8340−8343.

(4) Ayas, S.; Cupallari, A.; Ekiz, O. O.; Kaya, Y.; Dana, A. Counting Molecules with a Mobile Phone Camera Using Plasmonic Enhancement. *ACS Photonics* **2014**, *1*, 17−26.

(5) Homola, J.; Yee, S. S.; Gauglitz, G. Surface Plasmon Resonance Sensors: Review. *Sens. Actuators, B* **1999**, *54*, 3−15.

(6) Ji, N.; Ruan, W.; Wang, C.; Lu, Z.; Zhao, B. Fabrication of Silver Decorated Anodic Aluminum Oxide Substrate and Its Optical Properties on Surface-Enhanced Raman Scattering and Thin Film Interference. *Langmuir* **2009**, *25*, 11869−11873.

(7) Zhan, Z.; Lei, Y. Sub-100-nm Nanoparticle Arrays with Perfect Ordering and Tuneable and Uniform Dimensions Fabricated by Combining Nanoimprinting with Ultrathin Alumina Mambrane Technique. *ACS Nano* **2014**, *8*, 3862−3868.

(8) Dhathathreyan, A. Real-Time Monitoring of Invertase Activity Immobilized in Nanoporous Aluminum Oxide. *J. Phys. Chem. B* **2011**, *115*, 6678−6682.

(9) Hiep, H. M.; Yoshikawa, H.; Tamiya, E. Interference Localized Surface Plasmon Resonance Nanosensor Tailored for the Detection of Specific Biomolecular Interactions. *Anal. Chem.* **2010**, *82*, 1221−1227.

(10) Kim, D. K.; Kerman, K.; Saito, M.; Sathuluri, R. R.; Endo, T.; Yamamura, S.; Kwon, Y. S.; Tamiya, E. Label-Free DNA Biosensor Based on Localized Surface Plasmon Resonance Coupled with Interferometry. *Anal. Chem.* **2007**, *79*, 1855−1864.

(11) Yeom, S. H.; Kim, O. G.; Kang, B. H.; Kim, K. J.; Yuan, H.; Kwon, D. H.; Kim, H. R.; Kang, S. W. Highly Sensitive Nano-Porous Lattice Biosensor Based on Localized Surface Plasmon Resonance and Interference. *Opt. Express* **2011**, *19*, 22882−22891.

(12) Lau, K. H. A.; Duran, H.; Knoll, W. In Situ Characterization of *N*-Carboxy Anhydride Polymerization in Nanoporous Anodic Alumina. *J. Phys. Chem. B* **2009**, *113*, 3179−3189.

(13) Hotta, K.; Yamaguchi, A.; Teramae, N. Nanoporous Waveguide Sensor with Optimized Nanoarchitectures for Highly Sensitive Label-Free Biosensing. *ACS Nano* **2012**, *6*, 1541−1547.
(14) Lau, K. H. A.; Tan, L. S.; Tamada, K.; Sander, M. S.; Knoll, W. Highly Sensitive Detection of Processes Occurring inside Nanoporous Anodic Alumina Templates: A Waveguide Optical Study. *J. Phys. Chem. B* **2004**, *108*, 10812−10818.
(15) Fan, Y.; Hotta, K.; Yamaguchi, A.; Teramae, N. Enhanced Fluorescence in a Nanoporous Waveguide and Its Qualitative Analysis. *Opt. Express* **2012**, *20*, 12850−12859.
(16) Lee, S. J.; Guan, Z.; Xu, H.; Moskovits, M. Surface-Enhanced Raman Spectroscopy and Nanogeometry: The Plasmonic Origin of SERS. *J. Phys. Chem. C* **2007**, *111*, 17985−17988.
(17) Albrecht, C.; Kaeppel, N.; Gauglitz, G. Two Immunoassay Formats for Fully Automated CRP Detection in Human Serum. *Anal. Bioanal. Chem.* **2008**, *391*, 1845−1852.
(18) Leopold, N.; Busche, S.; Gauglitz, G.; Lendl, B. IR Absorption and Reflectometric Interference Spectroscopy (RIfS) Combined to a New Sensing Approach for Gas Analytes Absorbed into Thin Polymer Films. *Spectrochim. Acta, Part A* **2009**, *72*, 994−999.
(19) Orosco, M. M.; Pacholski, C.; Sailor, M. J. Real-Time Monitoring of Enzyme Activity in a Mesoporous Silicon Double Layer. *Nat. Nanotechnol.* **2009**, *4*, 255−258.
(20) Alvarez, S. D.; Li, C. P.; Chiang, C. E.; Schuller, I. K.; Sailor, M. J. A Label-Free Porous Alumina Interferometric Immunosensor. *ACS Nano* **2009**, *3*, 3301−3307.
(21) Dronov, R.; Jane, A.; Shapter, J. G.; Hodges, A.; Voelcker, N. H. Nanoporous Alumina-Based Interferometric Transducers Ennobled. *Nanoscale* **2011**, *3*, 3109−3114.
(22) Kumeria, T.; Santos, A.; Losic, D. Ultrasensitive Nanoporous Interferometric Sensor for Label-Free Detection of Gold(III) Ions. *ACS Appl. Mater. Interfaces* **2013**, *5*, 11783−11790.
(23) Santos, A.; Kumeria, T.; Losic, D. Optically Optimized Photoluminescent and Interferometric Biosensors Based on Nanoporous Anodic Alumina: A Comparison. *Anal. Chem.* **2013**, *85*, 7904−7911.
(24) Masuda, H.; Fukuda, K. Ordered Metal Nanohole Arrays Made by a Two-Step Replication of Honeycomb Structures of Anodic Alumina. *Science* **1995**, *268*, 1466−1468.
(25) Masuda, H.; Hasegwa, F.; Ono, S. Self-Ordering of Cell Arrangement of Anodic Porous Alumina Formed in Sulfuric Acid Solution. *J. Electrochem. Soc.* **1997**, *144*, L127−L130.
(26) Masuda, H.; Yada, K.; Osaka, A. Self-Ordering of Cell Configuration of Anodic Porous Alumina with Large-Size Pores in Phosphoric Acid Solution. *Jpn. J. Appl. Phys.* **1998**, *37*, L1340−L1342.
(27) Nielsch, K.; Choi, J.; Schwirn, K.; Wehspohn, R. B.; Gösele, U. Self-Ordering Regimes of Porous Alumina: The 10% Porosity Rule. *Nano Lett.* **2002**, *2*, 677−680.
(28) Lee, W.; Ji, R.; Gösele, U.; Nielsch, K. Fast Fabrication of Long-Range Ordered Porous Alumina Membranes by Hard Anodization. *Nat. Mater.* **2006**, *5*, 741−747.
(29) Schwirn, K.; Lee, W.; Hillebrand, R.; Steinhart, M.; Nielsch, K.; Gösele, U. Self-Ordered Anodic Aluminum Oxide Formed by H_2SO_4 Hard Anodization. *ACS Nano* **2008**, *2*, 302−310.
(30) Lee, W.; Schwirn, K.; Steinhart, M.; Pippel, E.; Scholz, R.; Gösele, U. Structural Engineering of Nanoporous Anodic Aluminium Oxide by Pulse Anodization of Aluminium. *Nat. Nanotechnol.* **2008**, *3*, 234−239.
(31) Santos, A.; Kumeria, T.; Losic, D. Nanoporous Anodic Aluminum Oxide for Chemical Sensing and Biosensors. *TrAC, Trends Anal. Chem.* **2013**, *44*, 25−38.
(32) Kumeria, T.; Santos, A.; Losic, D. Nanoporous Anodic Alumina Platforms: Engineered Surface Chemistry and Structure for Optical Sensing Applications. *Sensors* **2014**, *14*, 11878−11918.
(33) Santos, A.; Kumeria, T.; Losic, D. Nanoporous Anodic Alumina: A Versatile Platform for Optical Biosensors. *Materials* **2014**, *7*, 4297−4320.
(34) Kumeria, T.; Santos, A.; Rahman, M. M.; Ferré-Borrull, J.; Marsal, L. F.; Losic, D. Nanoporous Anodic Alumina Rugate Filters for Sensing of Ionic Mercury: Toward Environmental Point-of-Analysis Systems. *ACS Appl. Mater. Interfaces* **2014**, *6*, 12971−12978.
(35) Rahman, M. M.; Marsal, L. F.; Pallarès, J.; Ferré-Borrull, J. Tuning the Photonic Stop Bands of Nanoporous Anodic Alumina-Based Distributed Bragg Reflectors by Pore Widening. *ACS Appl. Mater. Interfaces* **2013**, *5*, 13375−13381.
(36) Abràmoff, M. D.; Magalhaes, P. J.; Ram, S. J. Image Processing with ImageJ. *Biophotonics Int.* **2004**, *11*, 36−42.
(37) Yisen, L.; Yi, C.; Zhiyuan, L.; Xing, H.; Yi, L. Structural Coloring of Aluminum. *Electrochem. Commun.* **2011**, *13*, 1336−1339.
(38) Kumeria, T.; Rahman, M. M.; Santos, A.; Ferré-Borrull, J.; Marsal, L. F.; Losic, D. Structural and Optical Nanoengineering of Nanoporous Anodic Alumina Rugate Filters for Real-Time and Label-Free Biosensing Applications. *Anal. Chem.* **2014**, *86*, 1837−1844.
(39) Santos, A.; Balderrama, V. S.; Alba, M.; Formentín, P.; Ferré-Borrull, J.; Pallarès, J.; Marsal, L. F. Nanoporous Anodic Alumina Barcodes: Toward Smart Optical Biosensors. *Adv. Mater.* **2012**, *24*, 1050−1054.
(40) Pacholski, C.; Sartor, M.; Sailor, M. J.; Cunin, F.; Miskelly, G. M. Biosensing Using Porous Silicon Double-Layer Interferometers: Reflective Interferometric Fourier Transform Spectroscopy. *J. Am. Chem. Soc.* **2005**, *127*, 11636−11645.
(41) Pacholski, C.; Yu, C.; Miskelly, G. M.; Godin, D.; Sailor, M. J. Reflective Interferometric Fourier Transform Spectroscopy: A Self-Compensating Label-Free Immunosensor Using Double-Layers of Porous SiO_2. *J. Am. Chem. Soc.* **2006**, *128*, 4250−4252.
(42) Kilian, K. A.; Lai, L. M. H.; Magenau, A.; Cartland, S.; Böcking, T.; Girolamo, N. D.; Gal, M.; Gaus, K.; Gooding, J. J. Smart Tissue Culture: In Situ Monitoring of the Activity of Protease Enzymes Secreted from Live Cells Using Nanostructured Photonic Crystals. *Nano Lett.* **2009**, *9*, 2021−2025.
(43) Kilian, K. A.; Böcking, T.; Gaus, K.; Gal, M.; Gooding, J. J. Peptide-Modified Optical Filters for Detecting Protease Activity. *ACS Nano* **2007**, *1*, 355−361.
(44) Jani, A. M. Md.; Kempson, I. M.; Losic, D.; Voelcker, N. H. Dressing in Layers: Layering Surface Functionalities in Nanoporous Aluminum Oxide Membranes. *Angew. Chem., Int. Ed.* **2010**, *49*, 7933−7937.
(45) Hoang, C. V.; Oyama, M.; Saito, O.; Aono, M.; Nagao, T. Monitoring the Presence of Ionic Mercury in Environmental Water by Plasmon-Enhanced Infrared Spectroscopy. *Sci. Rep.* **2013**, *3*, No. 1175.
(46) Zhang, L.; Chang, H.; Hirata, A.; Wu, H.; Xue, Q. K.; Chen, M. Nanoporous Gold Based Optical Sensor for Sub-ppt Detection of Mercury Ions. *ACS Nano* **2013**, *7*, 4595−4600.